Journal of Solid State Chemistry **150,** 294–304 (2000)
doi:10.1006/jssc.1999.8594, available online at http://www.idealibrary.com on IDEAL®

Tunneled Intergrowth Structures in the Ga_2O_3–In_2O_3–SnO_2 System

D. D. Edwards,*,[1] T. O. Mason,† W. Sinkler,‡ L. D. Marks,† K. R. Poeppelmeier,§ Z. Hu,‖ and J. D. Jorgensen‖

*New York State College of Ceramics at Alfred University, Department of Ceramic Engineering and Materials Science, Alfred, New York 14802; †Department of Materials Sciences and Engineering, Northwestern University, Evanston, Illinois 60208; ‡Argonne National Laboratory West, Idaho Falls, Idaho 83403; §Department of Chemistry, Northwestern University, Evanston, Illinois 60208; and ‖Argonne National Laboratory, Argonne, Illinois 60439

Received August 13, 1999; in revised form November 24, 1999; accepted December 4, 1999

The structures of several Ga_2O_3–In_2O_3–SnO_2 phases were investigated using high-resolution electron microscopy, X-ray diffraction, and Rietveld analysis of time-of-flight neutron diffraction data. The phases, expressed as $Ga_{4-4x}In_{4x}Sn_{n-4}O_{2n-2}$ ($n = 6$ and 7–17, odd), are intergrowths between the β-gallia structure of $(Ga, In)_2O_3$ and the rutile structure of SnO_2. Samples prepared with $n \geq 9$ crystallize in $C2/m$ and are isostructural with intergrowths in the Ga_2O_3–TiO_2 system. Samples prepared with $n = 6$ and $n = 7$ are members of an alternative intergrowth series that crystallizes in $P2/m$. Both intergrowth series are similar in that their members possess 1-D tunnels along the b axis. The difference between the two series is described in terms of different crystallographic shear plane operations (CSP) on the parent rutile structure.

INTRODUCTION

Beta-gallia (β-Ga_2O_3) reacts with oxides possessing the rutile structure (SnO_2, GeO_2, and TiO_2) to form homologous compounds that can be expressed as $Ga_4M_{n-4}O_{2n-2}$, where M is Ge, Ti, or Sn and n is an odd integer greater than 5 (1–3). Numerous reports have indicated that $Ga_4M_{n-4}O_{2n-2}$ compounds result from the coherent intergrowth of β-gallia and rutile substructures, such that $[010]_\beta$ and $[001]_r$ are parallel to the $[010]_i$, where the subscripts β, r, and i refer to β-gallia, rutile, and the intergrowth structures, respectively (1–6). As a result of the arrangement between the β-gallia and rutile substructures, the intergrowth phases crystallize in $C2/m$ and are characterized by a short unit-cell vector, b_i, similar in dimension to b_β and c_r (~ 3 Å). Another common feature among the intergrowth compounds is the presence of tunnels parallel to the b axis. Figure 1, after Kahn *et al.* (3), illustrates idealized representations of several intergrowth structures in relation to the parent β-gallia and rutile structures. To facilitate drawing of the intergrowth structures in Fig. 1, the anion sublattice of the rutile structure is drawn as hexagonal close packed (hcp). In reality, the anion sublattice of the rutile structure is distorted hcp.

The stability of the intergrowth compounds varies from system to system. In the Ga_2O_3–TiO_2 system, several odd members with $5 < n < 51$ have been observed (1, 2), but the $n = 5$ and $n = 7$ are metastable with respect to $n = 9$ and Ga_2TiO_5 (2). In the Ga_2O_3–GeO_2 and Ga_2O_3–SnO_2 systems only the lower n members are stable, including α-Ga_4GeO_8, $Ga_4Ge_3O_{12}$, and Ga_4SnO_8 (3, 7). Moreover, only odd members of the series have been reported (1–6).

In a recent investigation of phase relations in the Ga_2O_3–In_2O_3–SnO_2 system, we identified several intergrowth phases that can be expressed as $Ga_4In_{4-4x}Sn_{n-4}O_{2n-2}$ ($n = 6$ and 7–19, odd) (8). This paper reports on the structural investigations of the new intergrowth phases and provides a structural model for the two distinct intergrowth series.

EXPERIMENTAL

Mixed oxide powders, corresponding to $Ga_{4-x}In_xSn_{n-4}O_{2n-2}$, ($0 \leq x \leq 2$; $n = 4$–9, all integers and $n = 11$–21, odd) were prepared using one of two methods. In the first method, appropriate amounts of dried Ga_2O_3, In_2O_3, and SnO_2 powders (>99.9% purity, cation basis, Aldrich Chemical Company, Inc.) were moistened with acetone and mechanically mixed in an agate mortar. In the second method, mixed-oxide powders were obtained by coprecipitation from solutions containing Ga, In, and Sn metal (>99.9% purity, Aldrich Chemical Company, Inc.). Mixed-metal stock solutions ($\sim$10 mg/ml) were prepared by dissolving quantities of Ga and In in concentrated nitric acid and diluting with deionized water. Individual samples were prepared by first placing weighed quantities of Sn (0.3–0.6 g) in $\sim$15 ml of concentrated HNO_3. After complete reaction of the Sn with the HNO_3, an appropriate quantity of the Ga and In stock solutions was transferred to the mixture

[1] To whom correspondence should be addressed. E-mail: dedwards@king.alfred.edu.

0022-4596/00 $35.00

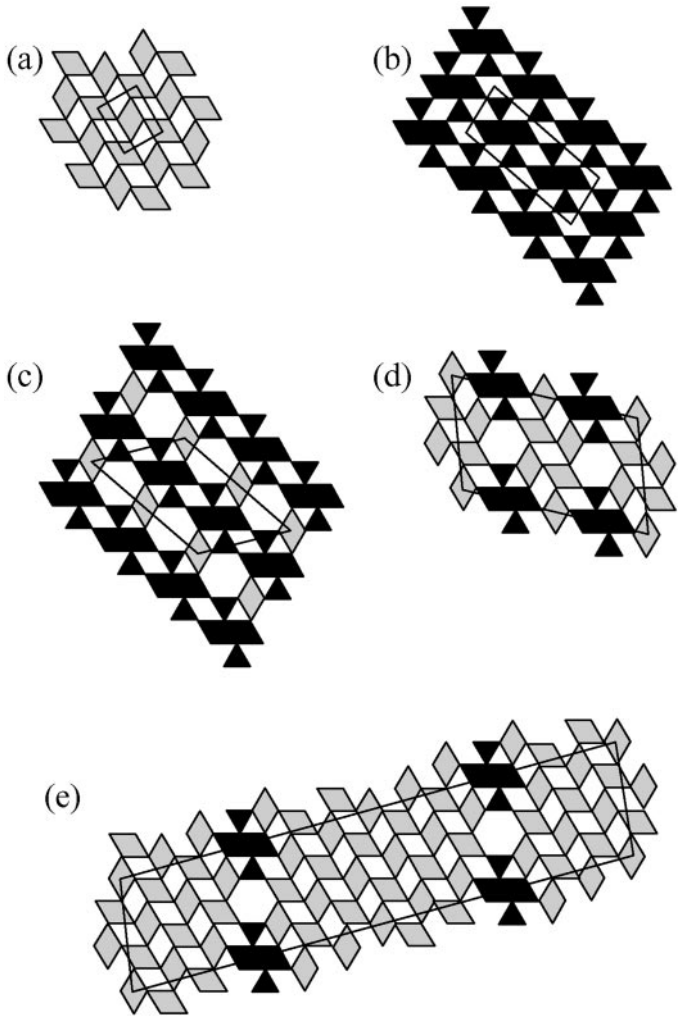

FIG. 1. Idealized two-dimensional projections of the crystal structures of (a) rutile, (b) β-Ga_2O_3, (c) Ga_4MO_8, M = Ge, Sn, (d) $Ga_4Ti_3O_{12}$, and (e) $Ga_4Ti_{21}O_{48}$.

resulting in a clear solution. Concentrated ammonium hydroxide was then added to the mixed solution to neutralize the acid and to precipitate the hydroxides. Excess water was removed from the samples by heating overnight at 110°C or for several days at room temperature. The dried product was heated slowly (1°C/minute) to 700°C in a porcelain crucible to remove the by-products and to convert the hydroxides into oxides. Mixed-oxide powders from both techniques were pressed into 1/2-inch pellets and heated for 3–60 days at 1150°C–1375°C, depending on the time needed to reach equilibrium. All samples were placed in high-density alumina crucibles, either surrounded by powder of the same composition or sandwiched between two sacrificial pellets of the same composition. After firing, samples were quenched in air. The samples were reground and reheated until equilibrium was achieved as determined by X-ray diffraction.

To prepare samples for X-ray diffraction, the pellets were ground into a fine powder using an agate mortar and pestle. A small amount of powder was applied to a glass slide using double-stick adhesive tape. For some samples, lithium fluoride was added as an internal standard. Diffraction studies were conducted on a Scintag diffractometer using Cu$K\alpha$ radiation (40 kV, 20 mA). Routine diffraction patterns were collected over 10–70° 2Θ in 0.05° steps, counting 1 s per step. Lattice parameters were determined using least-squares analysis.

High-resolution transmission electron microscopy (HRTEM) was performed using a Hitachi H9000 high-resolution electron microscope operated at 300 kV. Transmission electron diffraction (TED) data were obtained with a Hitachi HF2000 field emission analytical TEM, using a Gatan liquid-nitrogen-cooled specimen holder. The diffraction patterns were taken using a small probe positioned near the specimen edge. For specimen preparation, a small amount of powder was ground with a mortar and pestle under dry methanol to produce a suspension. A drop of the suspension was deposited on a 1000 mesh copper grid and dried. HRTEM images were taken as through-focus series, and images within the main Scherzer defocus interval were used to obtain approximate positions of cations. Direct methods using TED data combined with limited phase information from HRTEM was employed to obtain information regarding the oxygen atom positions (9–11). Direct-method calculations and image simulations were performed using software developed at Northwestern University.

Time-of-flight neutron diffraction was collected at Argonne National Laboratory's Intense Pulsed Neutron Source (12). Rietveld analysis of the neutron data was carried out using the GSAS (General Structural Analysis System) suite of programs (13). For neutron diffraction data, refined global parameters included the lattice parameters, up to 12 background coefficients, and 2 absorption coefficients. Of the 12 coefficients associated with the neutron peak-profile function, only 1 coefficient, related to peak width, was refined. Neutron scattering factors for Ga, In, Sn, and O were taken from the "International Tables of Crystallography" (14).

RESULTS AND DISCUSSION

The Ga_2O_3–In_2O_3–SnO_2 phase diagram, Fig. 2, illustrates the phase relations of the new intergrowth phases to SnO_2 and an extensive β-gallia solid solution, which can be expressed as $Ga_{2-2x}In_{2x}O_3$, $x < 0.43$ (8). Structural investigations were undertaken for samples prepared as $Ga_{4-4x}In_{4x}Sn_2O_{10}$, $Ga_{4-4x}In_{4x}Sn_3O_{12}$, and $Ga_{4-4x}In_{4x}Sn_5O_{16}$. These correspond to the phases labeled as $n = 6$, $n = 7$, and $n = 9$ in Fig. 2.

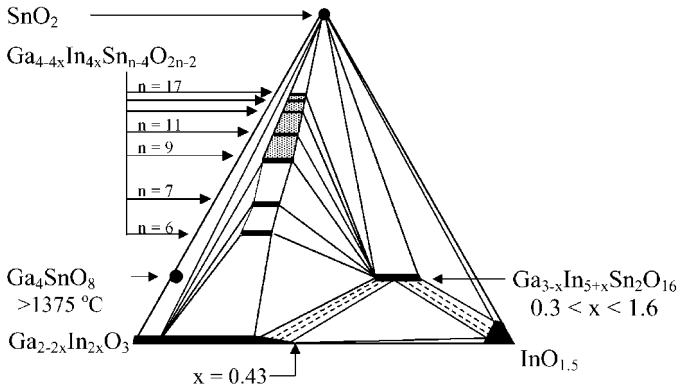

FIG. 2. The Ga_2O_3–In_2O_3–SnO_2 subsolidus phase diagram at 1250°C. Ga_4SnO_8 forms above 1375°C, but decomposes to Ga_2O_3 and SnO_2 at 1250°C.

Structural Determination of $Ga_{4-4x}In_{4x}Sn_2O_{10}$

Figure 3 shows a typical X-ray diffraction pattern for samples prepared as $Ga_{4-4x}In_{4x}Sn_2O_{10}$, $0.19 < x < 0.30$, which can be indexed to $P2/m$ as summarized in Table 1. Over the solid-solution range, the lattice parameters of $Ga_{4-4x}In_{4x}Sn_2O_{10}$ can be expressed as $a = 11.487 + 0.667x$ Å, $b = 3.098 + 0.237x$ Å, $c = 10.588 + 0.471x$ Å, and $\beta \sim 99°$.

Because of its monoclinic structure and short unit cell vector, $b \sim 3$ Å, the new phase was suspected to be an intergrowth between the β-gallia structure of $Ga_{2-2x}In_{2x}O_3$ and the rutile structure of SnO_2. However, the new phase crystallizes in $P2/m$ rather than $C2/m$, thereby corresponding to an even member ($n = 6$) of the series which is not allowed by the structural model presented by Kahn *et al.* (3)

Figure 4a is an HRTEM image of a $Ga_{4-4x}In_{4x}Sn_2O_{10}$ sample taken along [010], and Fig. 4b is an image calculated from a direct-methods technique that uses transmission electron diffraction (TED) intensities combined with low-resolution phase information from HRTEM images.

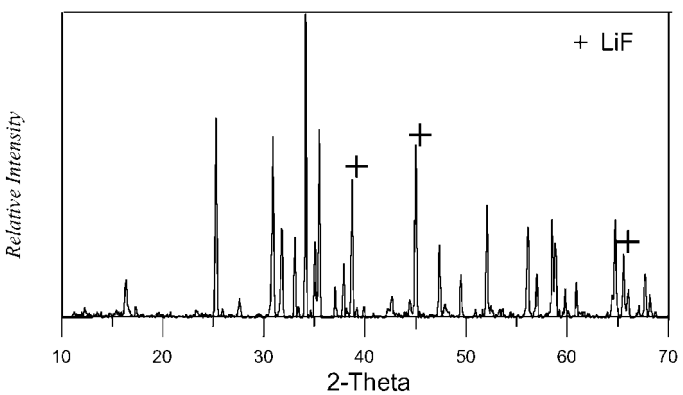

FIG. 3. An X-ray diffraction pattern of a $Ga_{4-4x}In_{4x}Sn_2O_{10}$ sample.

TABLE 1
Indexing of $Ga_{4-4x}In_{4x}Sn_2O_{10}$ X-Ray Powder Diffraction Patterns

			$x = 0.19$		$x = 0.22$		$x = 0.29$	
h	k	l	d (Å)	I/Io	d (Å)	I/Io	d (Å)	I/Io
2	0	0	5.7436	4	—	—	5.7643	5
−2	0	1	5.4036	16	5.4169	13	5.4353	12
−1	0	3	3.5161	57	3.5251	67	5.326	75
−2	0	3	3.2273	6	3.2332	6	3.2423	6
−4	0	1	2.8847	55	2.8945	59	2.9038	68
2	0	3	2.8098	29	2.8163	30	2.8232	27
−4	0	2	2.7006	22	2.7085	27	2.7171	26
−1	1	2	2.6755	4	2.6821	4	—	—
2	1	1	2.6192	100	2.6270	100	2.6360	100
−2	0	4	2.5528	24	2.5584	25	2.5650	22
−2	1	2	2.5240	53	2.5306	62	2.5394	59
−3	1	1	2.4189	7	2.4254	9	2.4329	7
−6	0	2	2.3685	12	2.3742	16	2.3804	14
−4	0	4	2.1158	9	2.1202	7	2.1266	7
4	1	1	2.0322	7	2.0382	6	2.0436	6
−4	1	3	1.9161	21	1.9194	23	1.9266	21
4	1	2	1.8953	6	1.8982	4	1.9047	6
−2	1	4	1.8382	13	1.8421	13	1.8471	14
0	1	5	1.7531	33	1.7565	35	1.7616	37
−6	1	0	1.6344	26	1.6388	30	1.6438	32
2	0	6	1.6313	17	1.6154	14	1.6200	16
0	2	0	1.5726	19	1.5767	30	1.5828	29
4	1	4	1.5656	28	1.5692	26	1.5744	27
−6	0	5	1.5432	8	1.5459	9	1.5507	10
3	1	5	1.5182	10	1.5204	11	1.5246	10
0	2	3	1.4372	28	1.4392	33	1.4441	34
7	1	1	1.4107	10	1.4144	9	—	—
−4	2	1	1.3801	13	1.3835	15	1.3895	10
2	2	3	1.3717	6	1.3750	7	1.3792	5

The technique, described in detail elsewhere, provides accurate estimates of the oxygen atom positions in the structure (9–11). The image is similar to those reported for Ga_2O_3–TiO_2 intergrowths in that it possesses large white spots that are interpreted as tunnels parallel to [010] (1, 2). The image defocus was estimated as -500 Å, based on characteristics of a faint amorphous component in the power spectrum. This defocus is within the extended Scherzer interval, thus, in thin regions, the image exhibits intensity minima (dark spots) corresponding to the projected cation positions. An idealized structural model, shown in Fig. 4c, was developed by considering the positions of the cations in relation to the tunnels. The model has 14 cation sites and 20 anion sites that can be placed in $P2/m$ as summarized in Table 2. Eight of the cation sites are associated with a β-gallia-like substructure, which is shown in gray in Fig. 4c. The remaining 6 cations reside at the center of rutile-like octahedra. A comparison of Figs. 4b and 4c shows that the positions of imaged oxygen atoms agree reasonably well with the oxygen positions in the idealized structure.

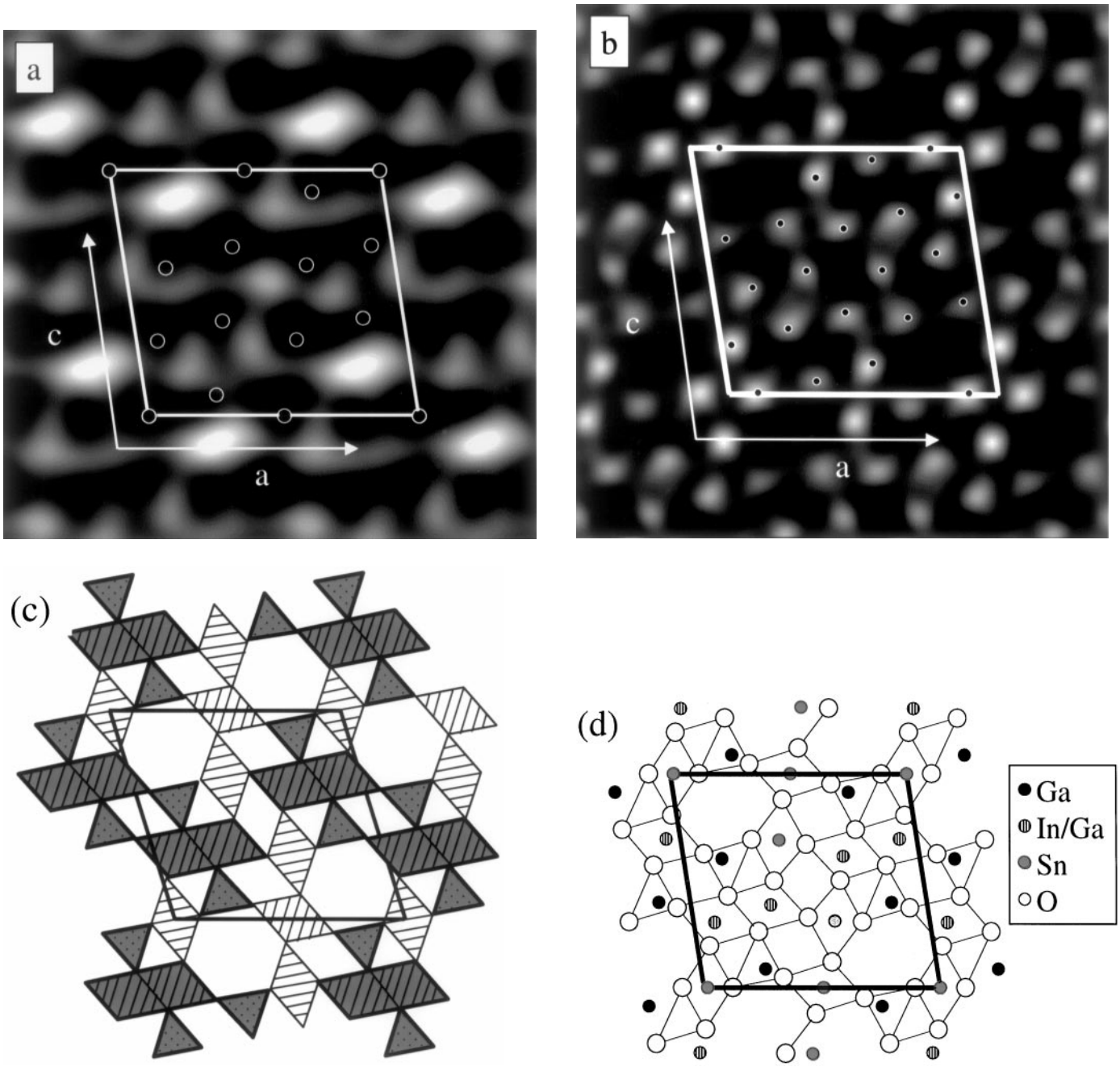

FIG. 4. Structure of $Ga_{4-4x}In_{4x}Sn_2O_{10}$ projected on (010): (a) an HRTEM image with cation positions highlighted; (b) the direct-methods solution with anion positions highlighted; (c) an idealized model showing polyhedra; (d) a ball-and-stick model with refined atom positions.

A Rietveld refinement of neutron data collected for a sample prepared as $Ga_{2.8}In_{1.2}Sn_2O_{10}$ was initiated with the cation positions obtained from the HRTEM image and the anion positions obtained from the direct-methods technique. During the refinement, Sn^{4+} was presumed to reside in the rutile-like octahedra, whereas Ga^{3+} and In^{3+} were presumed to reside in the β-gallia substructure. Because of its size, indium was presumed to reside only in the octahedral sites of the β-gallia substructure. The Ga/In occupancy of the β-gallia-like octahedra was constrained by the stoichiometry of the sample. As illustrated in Fig. 5, the refinement produced an excellent fit to the experimental data with $R_p = 4.95\%$ and $R_{wp} = 7.61\%$.

Structure Description of $Ga_{4-4x}In_{4x}Sn_2O_{10}$

A ball-and-stick projection of the refined $Ga_{4-4x}In_{4x}Sn_2O_{10}$ structure is shown in Fig. 4d. Crystallizing in $P2/m$ with

TABLE 2
Structural Parameters for $Ga_{2.8}In_{1.2}Sn_2O_{10}$[a]

Atom	Site	x	y	z	U*100 (Å)	Occupancy
Sn(1)	1*a*	0.0	0.0	0.0	1.20(30)	1.0
Sn(2)	1*b*	0.5	0.0	0.0	−0.04(20)	1.0
Sn(3)	2*e*	0.5923(6)	0.5	0.3112(7)	0.35(16)	1.0
In(4)	2*n*	0.3281(6)	0.0	0.3859(7)	0.09(25)	0.48(4)
Ga(4)	2*n*	0.3281(6)	0.0	0.3859(7)	0.09(25)	0.52(4)
In(5)	2*n*	0.0756(8)	0.5	0.3053(9)	1.10(30)	0.72(4)
Ga(5)	2*n*	0.0756(8)	0.5	0.3053(9)	1.10(30)	0.28(4)
Ga(6)	2*n*	0.1500(5)	0.0	0.6022(6)	0.94(18)	1.0
Ga(7)	2*n*	0.2624(5)	0.5	0.0869(5)	0.45(17)	1.0
O(1)	2*n*	0.3320(7)	0.0	0.0472(8)	1.09(24)	1.0
O(2)	2*n*	0.0365(6)	0.0	0.1941(8)	1.14(22)	1.0
O(3)	2*n*	0.4789(7)	0.0	0.3245(8)	1.37(24)	1.0
O(4)	2*n*	0.7096(6)	0.0	0.3076(6)	0.63(17)	1.0
O(5)	2*n*	0.1490(7)	0.0	0.4287(9)	1.77(17)	1.0
O(6)	2*n*	0.1081(7)	0.5	0.0003(7)	0.24(17)	1.0
O(7)	2*n*	0.5515(7)	0.5	0.1209(8)	0.60(23)	1.0
O(8)	2*n*	0.2570(6)	0.5	0.2617(8)	0.24(19)	1.0
O(9)	2*n*	0.3586(7)	0.5	0.4987(7)	0.96(19)	1.0
O(10)	2*n*	0.0768(6)	0.5	0.6272(6)	0.65(21)	1.0

$R_{wp} = 7.61\%$ $R_p = 4.95\%$ $\chi^2 = 2.164$

[a] Space group $P2/m$. $a = 11.68919(18)$ Å, $b = 3.16734(5)$ Å, $c = 10.73068(15)$ Å, $\beta = 98.9997(15)^\circ$.

$Z = 2$, $Ga_{4-4x}In_{4x}Sn_2O_{10}$ can be viewed as an intergrowth between the β-gallia structure of $Ga_{2-2x}In_{2x}O_3$ and the rutile structure of SnO_2. As with previously reported intergrowths, the structure of $Ga_{4-4x}In_{4x}Sn_2O_{10}$ possesses tunnels parallel to [010]. The tunnels are bound by two chains of Ga tetrahedra, three chains of Sn octahedra, and one chain of a Ga/In octahedra.

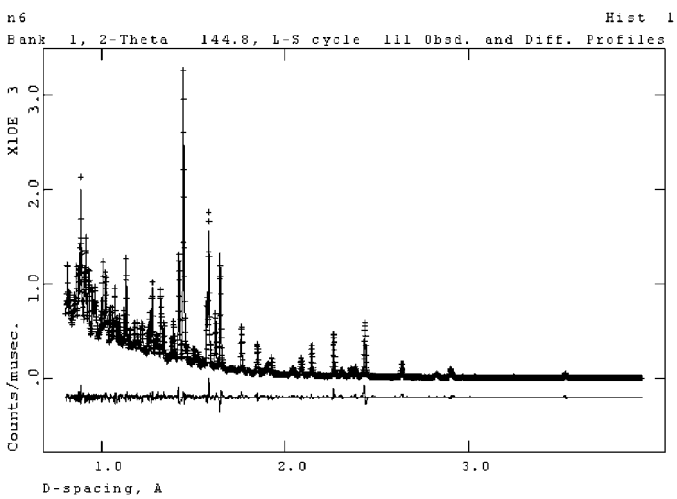

FIG. 5. Observed, calculated, and difference TOF neutron powder diffraction patterns for $Ga_{2.8}In_{1.2}$ Sn_2O_{10}. The observed and calculated data are indicated by crosses and by a solid line, respectively.

TABLE 3
Select Bond Lengths in $Ga_{2.8}In_{1.2}Sn_2O_{10}$

Polyhedra	Bond	Number	Length
SnO_6	M(1)–O(2)	2	2.0259(8)
	M(1)–O(6)	4	2.045(4)
	Average		2.050
SnO_6	M(2)–O(1)	2	2.099(8)
	M(2)–O(7)	4	2.066(4)
	Average		2.077
SnO_6	M(3)–O(3)	2	2.057(2)
	M(3)–O(4)	2	2.092(6)
	M(3)–O(7)	1	2.033(9)
	M(3)–O(9)	1	2.030(9)
	Average		2.030
$(In/Ga)O_6$	M(4)–O(3)	1	2.012(11)
	M(4)–O(5)	1	2.168(10)
	M(4)–O(6)	2	2.156(6)
	M(4)–O(9)	2	1.984(6)
	Average		2.077
$(In/Ga)O_6$	M(5)–O(2)	2	2.010(7)
	M(5)–O(5)	2	2.141(8)
	M(5)–O(8)	1	2.255(10)
	In(5)–O(10)	1	2.011(11)
	Average		2.095
GaO_4	M(6)–O(4)	1	1.765(9)
	M(6)–O(5)	1	1.898(9)
	M(6)–O(10)	2	1.851(5)
	Average		1.841
GaO_4	M(7)–O(5)	2	1.866(5)
	M(7)–O(7)	1	1.866(9)
	M(7)–O(9)	1	1.867(7)
	Average		1.866

The structure possesses cations with fourfold and sixfold coordination. Table 3 summarizes the M–O bond lengths associated with each of the coordination polyhedra. For comparison, Table 4 provides the M–O bond lengths of the component oxides (15–17). The average M–O bond lengths in the SnO_6 octahedra (2.0230–2.077 Å) are comparable to that found in SnO_2 (2.05 Å). The average bond lengths in $(Ga/In)O_6$ octahedra (2.077 and 2.095 Å) are somewhat

TABLE 4
Select Bond Lengths of Component Oxides

Bond	Coordination polyhedra	Compound	M–O bond length (Å)	Reference
Sn–O	MO_6	SnO_2	Average: 2.05	(17)
Ga–O	MO_4	Ga_2O_3	Range 1.80–1.85 Average: 1.83	(15)
Ga–O	MO_6	Ga_2O_3	Range: 1.95–2.08 Average: 2.00	(15)
In–O	MO_6	In_2O_3	Range: 2.13–2.23 Average: 2.18	(16)

larger than those found in the β-gallia octahedra, but not unreasonably large considering the extensive substitution of In in the β-gallia substructure. The average M–O bond lengths in the GaO_4 tetrahedra (1.841 and 1.866 Å) are similar to the average found in the β-gallia structure (1.83 Å). However, while one of the tetrahedra is nearly regular, the other is severely distorted with bond lengths ranging from 1.765 to 1.898 Å.

Structural Investigation of n = 7 Intergrowth

Figure 6 shows a typical X-ray diffraction pattern of samples prepared as $Ga_{4-x}In_xSn_{n-4}O_{2n-2}$, $n = 7$. Like the $n = 6$ phase, the $n = 7$ phase can be indexed to $P2/m$ as summarized in Table 5. Over the solubility range, the lattice parameter of $Ga_{4-4x}In_{4x}Sn_3O_{12}$ can be expressed as $a = 14.181 + 0.784x$ Å, $b = 3.115 + 0.202x$ Å, $c = 10.582 + 0.435x$ Å, $\beta = 108 - 0.98x^\circ$.

Like the $n = 6$ samples, the $n = 7$ samples were suspected to be intergrowths between the β-gallia structures of $Ga_{2-2x}In_{2x}O_3$ and the rutile structure of SnO_2. Although the stoichiometry was consistent with phases reported for the Ga_2O_3–TiO_2 and Ga_2O_3–GeO_2 systems (1–3), the new $n = 7$ phase crystallizes in $P2/m$ rather than $C2/m$.

A structural model was developed for the $n = 7$ phase based on HRTEM images and the direct methods technique. Figures 7a–7c show three consecutive HRTEM images of the $n = 7$ phase from a through-focus series. The defocus for Fig. 7a was estimated as -600 Å using a faint amorphous component in the image power spectrum. This defocus is within the extended Scherzer interval for the instrument used. As in the case of the $n = 6$ phase, the large white spots are interpreted as tunnels parallel to the b axis, and the intensity minima are attributed to columns of cations. Probable anion locations were determined from direct-methods solutions, two of which are shown in Figs. 7d and 7e. These solutions show the approximate positions of 22 of the 24 anions required by the stoichiometry of the phase. An idealized model, Fig. 7f, was deduced from the experimental images. Using cation positions estimated from the HRTEM image, multislice image simulations were computed and are shown as insets to Figs. 7a–7c. The image calculations were performed for small thicknesses—a single unit cell along the b axis—and may be compared with the experimental images in regions just adjacent to the specimen edge (see outlined unit cells). The good agreement between features of the experimental and calculated images provides confirmation of the proposed structural model shown (Fig. 7f).

TABLE 5
Indexing of $Ga_{4-4x}In_{4x}Sn_3O_{12}$ X-Ray Powder Diffraction Patterns

			$x = 0.20$		$x = 0.25$		$x = 0.29$	
h	k	l	d (Å)	I/Io	d (Å)	I/Io	d (Å)	I/Io
2	0	1	4.9461	11	4.9679	8	4.9751	11
3	0	1	3.7086	7	3.7246	6	3.7300	7
−2	0	3	3.4953	60	3.5027	51	3.5080	58
−3	0	3	3.2450	11	3.2540	10	3.2575	10
4	0	1	2.9455	60	2.9577	52	2.9623	54
−4	0	3	2.9000	22	2.9082	18	2.9109	22
−1	1	2	2.7126	19	2.7228	16	2.7275	18
0	1	2	2.6751	9	2.6849	8	2.6895	8
−3	1	1	2.6248	100	2.6346	100	2.6386	100
1	1	2	2.5443	59	2.5546	53	2.5585	60
0	0	4	2.5245	22	2.5317	17	2.5367	21
3	1	1	2.4023	6	2.4116	5	2.4155	6
−6	0	2	2.3672	15	2.3738	15	2.3775	15
6	0	0	—	—	2.2698	4	2.2739	4
2	0	4	2.1529	6	2.1589	5	2.1633	5
3	1	3	1.8920	16	1.8983	13	1.9016	17
6	0	2	1.8555	6	1.8623	4	1.8650	6
−6	1	3	1.8277	14	1.8330	12	1.8351	13
−3	1	5	1.7568	36	1.7613	31	1.7640	33
−1	1	5	1.7485	4	1.7517	5	1.7550	4
4	1	3	1.7370	4	—	—	1.7456	4
−7	1	2	1.7155	6	1.7194	5	1.7225	5
3	0	5	1.6527	30	1.6588	25	1.6616	25
−6	0	6	1.6235	15	1.6272	12	1.6289	14
5	1	3	—	—	1.6001	13	1.6025	19
0	2	0	1.5773	19	1.5833	20	1.5861	19
4	0	5	1.5344	8	1.5388	7	1.5418	8
−4	0	7	1.5141	9	1.5179	10	1.5201	9

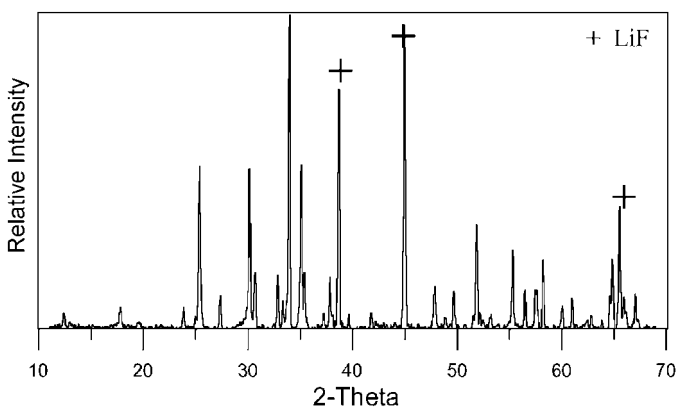

FIG. 6. An X-ray diffraction pattern of a $Ga_{4-4x}In_{4x}Sn_3O_{12}$ sample.

Structural Investigation of n > 9 (odd) Intergrowths

Figure 8 compares the X-ray diffraction patterns of samples prepared as $Ga_{4-x}In_xSn_{n-4}O_{2n-2}$ with $n \geq 9$ (odd) and with $0.20 \leq x \leq 0.25$. The diffraction patterns of $n \geq 9$ samples are very similar to one another, possessing a few well-defined peaks that are similar to those found in the X-ray diffraction pattern of SnO_2. The diffraction patterns also possess a number of broad, ill-defined peaks, the position of

which varies systematically with n. The presence of broad, ill-defined peaks suggests that the samples are not well crystallized. Continued heating of the samples at 1250 and 1375°C had little effect on the resulting diffraction patterns. In a study of Ti-rich Ga_2O_3–TiO_2 intergrowths, Kamiya and Tilley also reported ill-defined diffraction patterns and samples that failed to achieve equilibrium, which they attributed to loss of Ga_2O_3 at the surface (1).

Although ill defined, the diffraction patterns of the $n = 9$ samples could be indexed to a $C2/m$ unit cell as summarized in Table 6. Over the solid-solubility range, the lattice parameters of $Ga_{4-x}In_xSn_5O_{16}$ can be expressed as

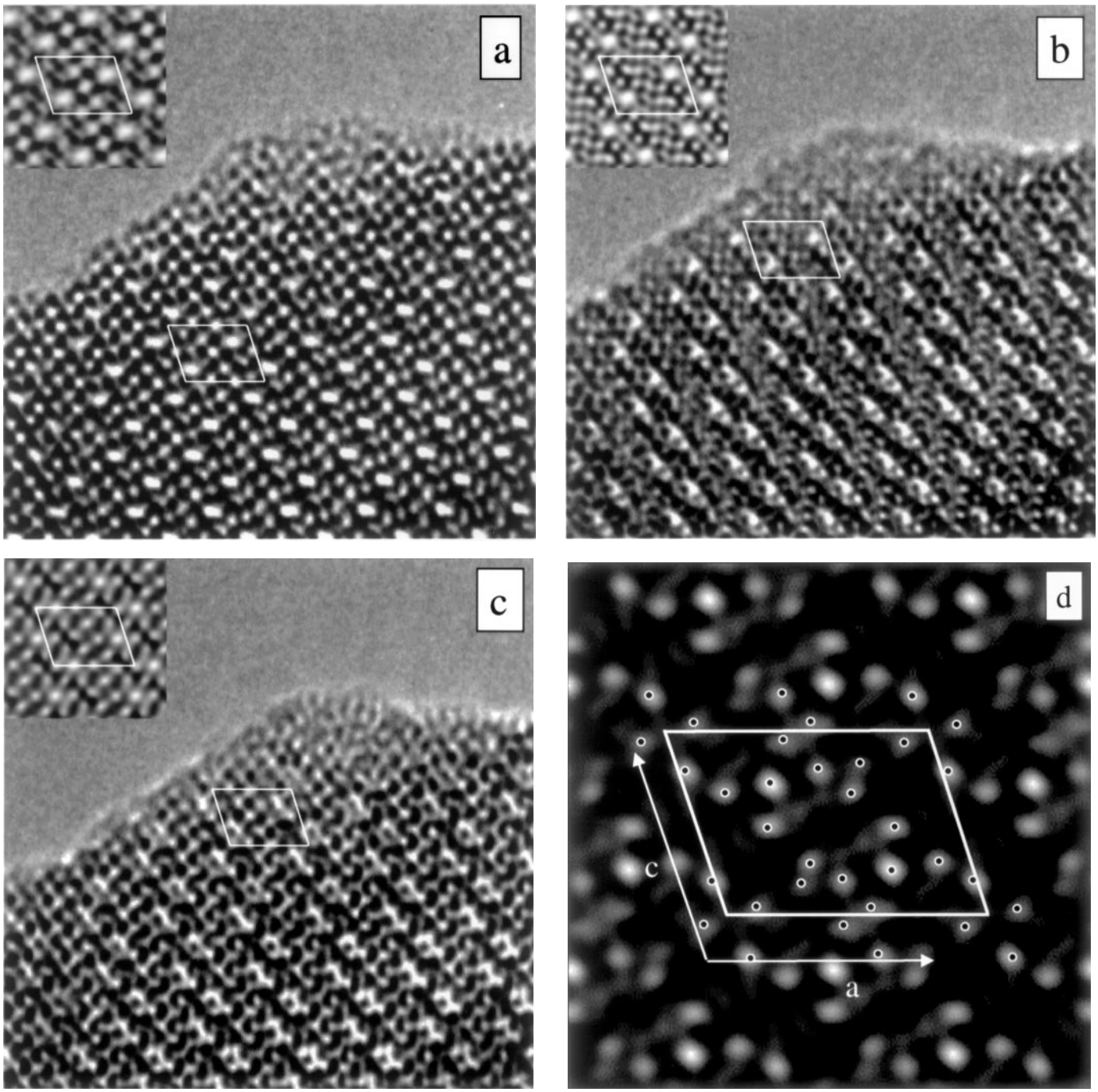

FIG. 7. Structure of $Ga_{4-4x}In_{4x}Sn_2O_{10}$ projected on (010): (a–c) HRTEM images taken from a through focus series at defoci (a) −600 Å, (b) −700 Å, and (c) −850 Å with image calculations for one unit cell, or a thickness of 3.2 Å shown as insets; (d) direct-methods solutions indicating 18 of the 24 anion positions, (e) direct-methods solution indicating 4 of the 24 anion positions, (f) an idealized model showing polyhedra.

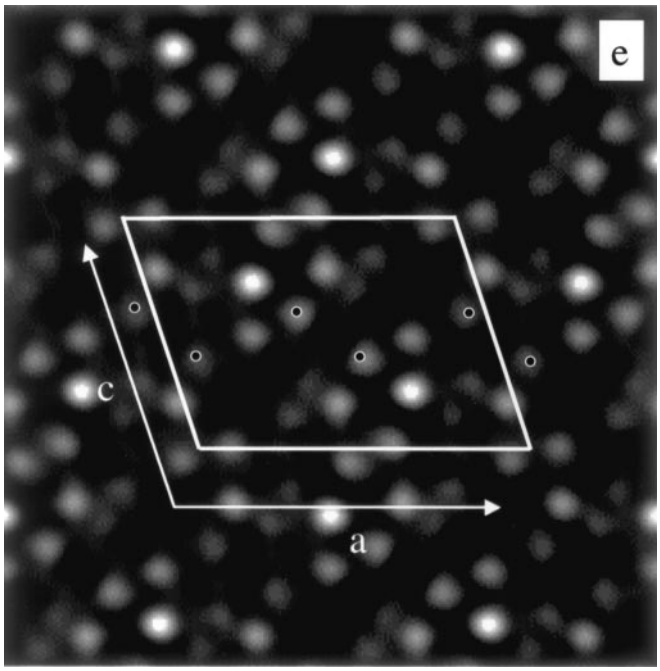

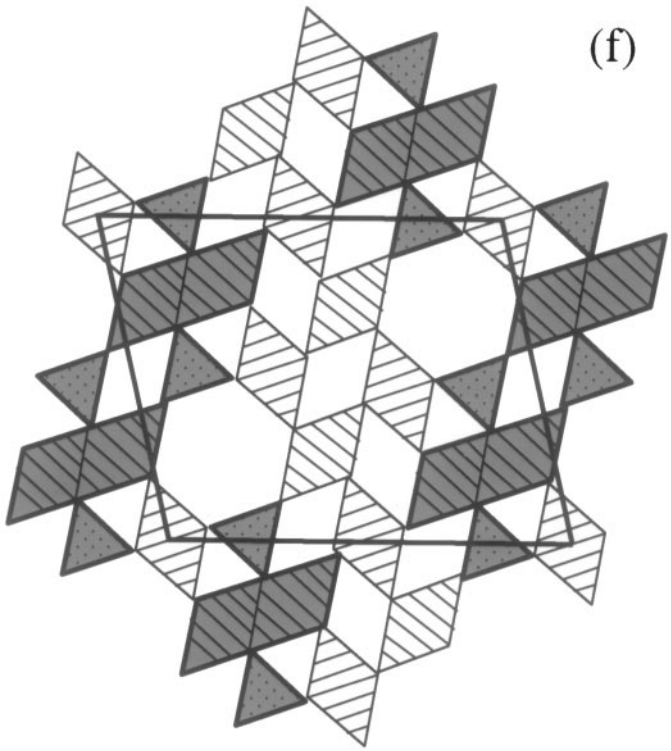

FIG. 7—*Continued*

$a = 18.107 + 0.651x$ Å, $b = 3.139 + 0.128x$ Å, $c = 10.580 + 0.261x$ Å, and $\beta = 102.2–0.97x^\circ$. These parameters are somewhat larger than those reported for $Ga_4Ti_5O_{16}$ ($a = 17.76$ Å, $b = 2.96$ Å, $c = 10.3$ Å, $\beta = 103.2^\circ$) as expected from a comparison of the average cation radii.

Figure 9 shows an HRTEM image of a sample with composition corresponding to $n = 9$. As with previously discussed images, the large white features are interpreted as tunnels along [010] in the intergrowth structures (See Fig. 1). Two phases, corresponding to different values of n, are present in the image as indicated by the outlined unit cells. Boundaries separating the two phases are also indicated. The short coherence length along the a^* axis caused pronounced streaking, which prevented accurate measurement of diffraction intensities for direct methods. Nevertheless, model structures for both phases could be obtained from the HRTEM images.

The smaller of the two unit cells outlined in Fig. 9 corresponds to $(Ga,In)_4Sn_5O_{16}$. The a/c ratio measured from the image was in good agreement with the X-ray diffraction data and was similar to that reported for $Ga_4Ti_5O_{16}$. Moreover, the relative placement of the tunnels with respect to each other is consistent with the structural model reported for $Ga_4Ti_5O_{16}$ (2).

A portion of the image containing the second, larger structure was digitally averaged and is shown as Fig. 10a. Again, the large white spots and smaller dark spots are interpreted as tunnels and cations, respectively. The model shown as Fig. 10b was constructed from the approximate cation positions. The structure is consistent with the $n = 11$ member of the series. While a cursory investigation of the sample did not reveal any structures with $n < 9$, such structures are expected since the overall composition of the sample corresponds to $n = 9$.

Comparison of the Intergrowth Structures

Several homologous phases were observed in the Ga_2O_3–In_2O_3–SnO_2 system. The phases, expressed as $Ga_{4-4x}In_{4x}Sn_{n-4}O_{2n-2}$, are similar to one another in that they crystallize in monoclinic structures with a short unit-cell vector ($b \sim 3$ Å) and tunnels parallel to the b axis. Nevertheless, the phases belong to two distinct homologous series. The two series are distinguished from one another by different arrangements of the β-gallia and rutile components within the structure, which results in one series crystallizing in $C2/m$ and the other crystallizing in $P2/m$. The observed $C2/m$ structures are isostructural with those reported in the Ga_2O_3–TiO_2 system. The $P2/m$ structures with $n = 6$ and $n = 7$ have not been reported previously.

Figure 11 illustrates the fundamental difference between the two series in terms of crystallographic shear plane

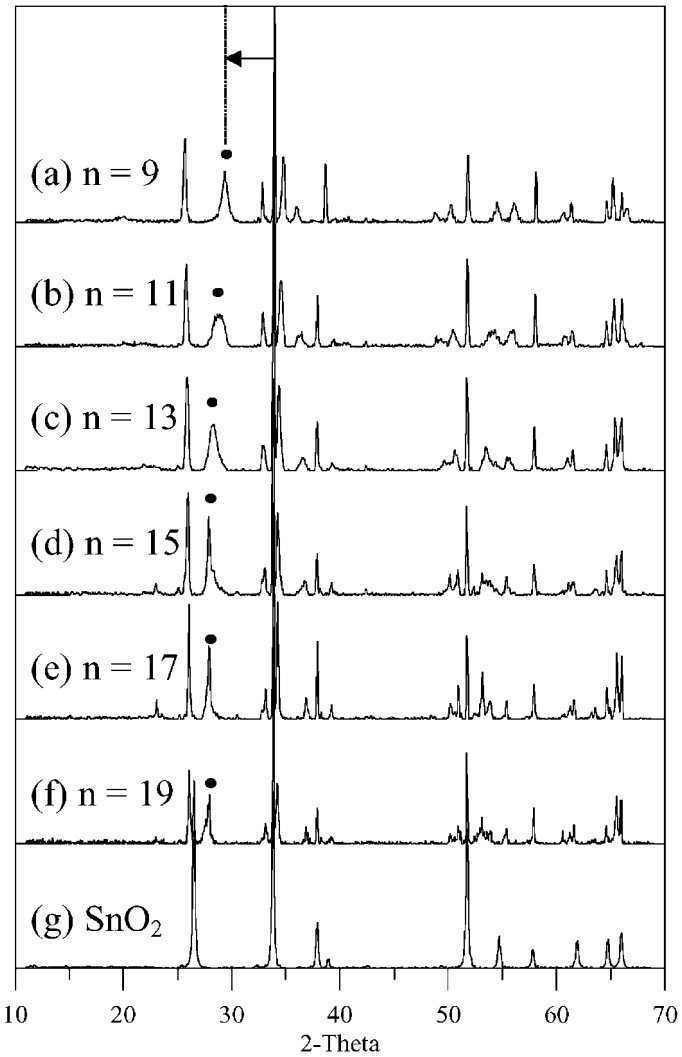

FIG. 8. X-ray diffraction patterns of samples prepared as $Ga_{4-4x}In_{4x}Sn_{n-4}O_{2n-2}$; $0.20 < x < 0.25$, $n > 9$, odd.

operations on the rutile structure. The $C2/m$ structure results from a $(210)_r[1/2, 1/4, 1/2]_r$ operation on the rutile structure with insertion of $(Ga, In)_2O_3$ units at the boundary between the rutile slabs. The $P2/m$ structure results from a $(210)_r[0, 1/2, 0]_r$ operation with insertion of $(Ga, In)_4SnO_8$ units at the boundary. An important consequence of the differences in the CSP operations and boundary composition is that the $P2/m$ series can assume all integral values of n in the formula $(Ga, In)_4Sn_{n-4}O_{2n-2}$, whereas the $C2/m$ series can only assume odd values of n. Although both boundary structures had been observed previously in the Ga_2O_3–TiO_2 system, the periodic repetition of the $(210)_r[0, 1/2, 0]_r$ boundary was not observed, thus no even-member phases were reported. It is interesting to note that the $n = 5$ structure possesses elements of both boundary structures and is the first member of both series.

TABLE 6
Indexing of $Ga_{4-4x}In_{4x}Sn_5O_{16}$ X-Ray Powder Diffraction Patterns

			$x = 0.20$		$x = 0.25$		$x = 0.29$	
h	k	l	d (Å)	I/Io	d (Å)	I/Io	d (Å)	I/Io
−4	0	1	4.4402	4	—	—	4.4583	4
0	0	3	3.4614	42	3.4641	42	3.4697	49
−6	0	1	3.0333	24	3.0368	25	3.0423	26
−1	1	2	2.7167	18	2.7212	18	2.7255	19
3	1	1	2.6302	100	2.6353	100	2.6404	100
−3	1	2	2.5732	33	2.5763	33	2.5821	40
−4	0	4	2.4868	8	2.4914	8	2.4939	8
5	1	0	2.3664	17	2.3704	18	2.3736	18
−7	1	3	1.8587	6	1.8634	5	1.8657	6
3	1	4	1.8111	7	1.8139	9	1.8154	9
−1	1	5	1.7600	28	1.7621	31	1.7648	34
−9	1	0	1.6787	8	1.6813	9	1.6838	14
6	1	4	1.6354	10	1.6377	10	1.6400	14
−9	1	3	1.6239	4	—	—	1.6319	5
0	2	0	1.5823	18	1.5857	22	1.5885	21
−10	0	5	1.5227	5	1.5260	5	1.5285	5
−4	0	7	1.5080	9	1.5095	9	1.5118	7
0	2	3	1.4378	10	1.4407	10	1.4435	12
−7	1	6	—	—	1.4293	21	1.4314	20
9	1	3	1.4105	11	1.4137	13	1.4157	14
−6	2	1	1.4023	7	1.4050	7	1.4070	7

Table 7 illustrates that the number of stable intergrowth phases in a system can be roughly correlated to the extent of lattice matching between the $\mathbf{b}_\beta$ lattice parameter of β-gallia component and the $\mathbf{c}_r$ lattice parameter of the rutile component. Among the binary-oxide systems listed, the Ga_2O_3–TiO_2 system has the smallest mismatch (<3% with $\mathbf{b}_\beta > \mathbf{c}_r$) and the largest number of reported intergrowths. In the Ga_2O_3–GeO_2 system, where $\mathbf{b}_\beta$ is approximately 6% larger than $\mathbf{c}_r$, only two intergrowth phases (Ga_4GeO_8 and $Ga_4Ge_3O_{12}$) have been reported. In the Ga_2O_3–SnO_2 system, where $\mathbf{b}_\beta$ is approximately 5% smaller than $\mathbf{c}_r$, only one intergrowth phase (Ga_4SnO_8) has been reported.

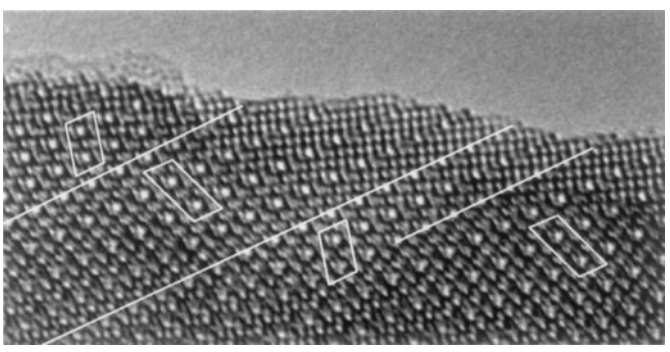

FIG. 9. An HRTEM image of a sample prepared as $Ga_{4-4x}In_{4x}Sn_5O_{18}$

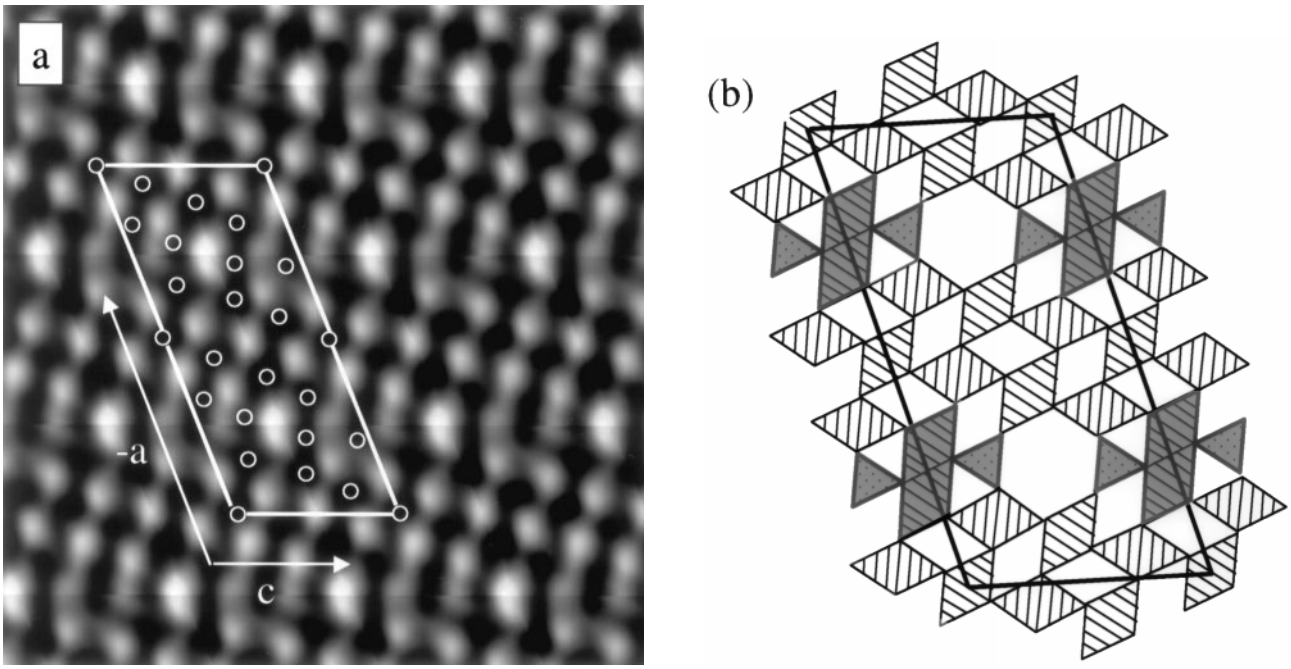

FIG. 10. Structure of $Ga_{4-4x}In_{4x}Sn_7O_{20}$ projected on (010): (a) HRTEM image with cation positions highlighted and (b) an idealized model showing polyhedra.

Incorporating indium into the β-gallia structure increases $\mathbf{b}_\beta$ from 3.04 Å for Ga_2O_3 to 3.15 Å for $Ga_{1.4}In_{0.6}O_3$ and reduces the mismatch between $\mathbf{b}_\beta$ and $\mathbf{c}_r$ of SnO_2. Over the stability ranges of the $Ga_{4-4x}In_{4x}Sn_{n-4}O_{2n-2}$ phases, $\mathbf{b}_\beta$ is approximately 1–3% smaller than $\mathbf{c}_r$.

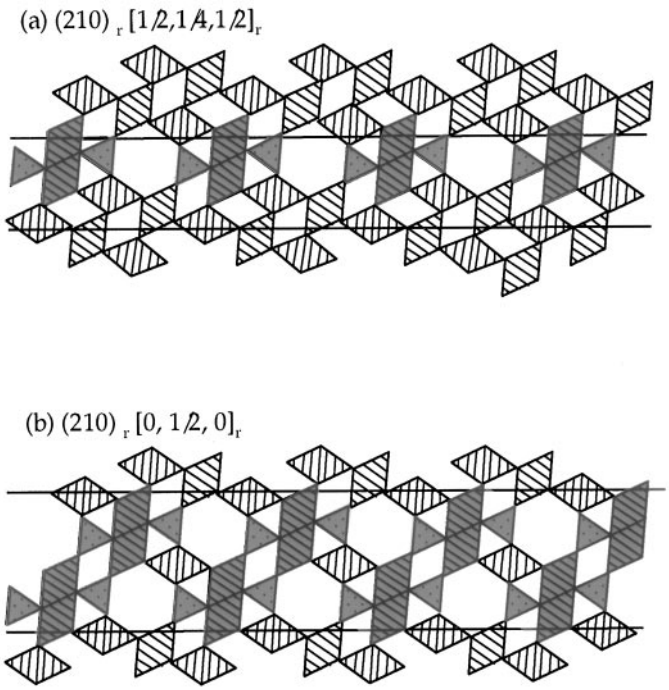

FIG. 11. Idealized models of the boundary structure in (a) the $C2/m$ and (b) the $P2/m$ intergrowth series.

Two intriguing questions are presented by the current work. First, can higher n members of the $P2/m$ intergrowth series be prepared? To date, only the $n = 6$ and $n = 7$ members of the $P2/m$ intergrowth structure have been observed. While higher n members were observed in the Ga_2O_3–In_2O_3–SnO_2 system, they adopted the $C2/m$ rather than the $P2/m$ structure. Second, does the presence of different sized cations in the β-gallia substructure play some role in the stabilization of the $P2/m$ structures? Although intergrowth structures are abundant in the Ga_2O_3–TiO_2 system, no $P2/m$ structures have been observed. Further studies involving variations in the rutile component and systematic substitutions of the β-gallia component are suggested as a possible means of exploring these questions.

CONCLUSIONS

The structures of several related phases, expressed as $Ga_{4-4x}In_{4x}Sn_{n-4}O_{2n-2}$ ($n = 6$ and 7–17, odd), were investigated using a battery of techniques, including transmission electron microscopy, X-ray diffraction, and time-of-flight neutron diffraction. The investigated phases are intergrowths between the β-gallia structure of $(Ga,In)_2O_3$ and the rutile structure of SnO_2. Although all of the phases are similar in that they possess tunnels parallel to the b axis of a monoclinic structure, they belong to two distinct homologous series. Phases with $n \geq 9$ (odd) crystallize in $C2/m$

TABLE 7
Comparison of Intergrowth Systems

β-gallia component	b_β (Å)	Rutile component	c_r (Å)	$(b_\beta - c_r)/b_\beta$	Reported intergrowths	Reference
Ga_2O_3	3.04	GeO_2	2.860	+ 0.059	$n = 5, 7$	(3)
Ga_2O_3	3.04	TiO_2	2.959	+ 0.027	$n = 9$–51, odd	(1–3, 5, 6)
Ga_2O_3	3.04	SnO_2	3.185	− 0.048	$n = 5$	(7)
$Ga_{1.4}In_{0.6}O_3$	3.15	SnO_2	3.185	− 0.011	$n = 6$, 7–17, odd	(8)

and are isostructural with phases in the Ga_2O_3–TiO_2 system. Phases with $n = 6$ and $n = 7$ crystallize in $P2/m$ and possess no known analogs. The difference between the two series was described in terms of different crystallographic shear plane operations on the parent rutile structure.

ACKNOWLEDGMENTS

This work was supported by and largely conducted in the facilities of the Materials Research Center at Northwestern University with the support of the National Science Foundation under MRSEC Grant DMR-9632472. The support of the National Science Foundation through the Science and Technology Center for Superconductivity (DMR 91-20000) is also gratefully acknowledged (W.S. and L.D.M.). Some of the work was carried out at the Intense Pulsed Neutron Source at Argonne National Laboratory, which is funded by the U.S. Department of Energy under Contract W-31-109-ENG-38.

REFERENCES

1. S. Kamiya and R. J. D. Tilley, *J. Solid State Chem.* **22,** 205 (1977).
2. L. A. Bursill and G. G. Stone, *J. Solid State Chem.* **38,** 149 (1981).
3. A. Kahn, V. Agafonov, D. Michel, and M. Perez Y Jorba, *J. Solid State Chem.* **65,** 377 (1986).
4. G. G. Stone and L. A. Bursill, *Philos. Mag.* **35**(5), 1397 (1977).
5. L. A. Bursill and G. G. Stone, *Philos. Mag.* **32,** 1151 (1975).
6. D. J. Lloyd, I. E. Grey, and L. A. Bursill, *Acta Crystallogr. Sect. B* **32,** 1756 (1976).
7. M. B. Varfolomeev, A. S. Mironova, T. I. Dudina, and N. D. Koldashov, *Zh. Neorg. Khim.* **20,** 3140 (1975).
8. D. D. Edwards and T. O. Mason, *J. Am. Ceram. Soc.* **81**(12), 3285 (1998).
9. W. Sinkler, L. D. Marks, D. D. Edwards, T. O. Mason, K. R. Poeppelmeier, Z. Hu, and J. D. Jorgensen, *J. Solid State Chem.* **136,** 145 (1998).
10. W. Sinkler, E. Bengu, and L. D. Marks, *Acta Crystallogr. Sect. A* **54,** 591 (1998).
11. W. Sinkler and L. D. Marks, *Ultramicroscopy* **75,** 251 (1999).
12. J. D. Jorgensen, *J. Appl. Crystallogr.* **22,** 321 (1989).
13. A. C. Larson and R. B. Von Dreel, "General Structure Analysis System." Los Alamos National Laboratory, Los Alamos, NM.
14. A. C. Wilson, "International Tables for Crystallography," Vol. C. Kluwer Academic, Boston, 1995.
15. S. Geller, *J. Chem. Phys.* **33**(3), 676 (1960).
16. M. Marezio, *Acta Crystallogr.* **20,** 723 (1966).
17. V. W. H. Baur, *Acta Crystallogr.* **9,** 515 (1956).